IEEE Robotics and Automation Letters (RA-L) paper, presented at ICRA 2023, London, UK. Cite as RA-L paper.

UVtac: Switchable UV Marker-Based Tactile Sensing Finger for Effective Force Estimation and Object Localization

Woojong Kim, Won Dong Kim, Jeong-Jung Kim, Chang-Hyun Kim, and Jung Kim, *Member, IEEE*

***Abstract*—Vision-based tactile sensors provide diverse information of external tactile stimuli on the skin of sensors using both marker and reflective membrane images. However, when markers and reflective membranes are used concurrently, conventional opaque markers inevitably disturb the camera's view of the reflective membrane. Thus, simultaneously increasing the quality of tactile information extracted from each visual feature has remained a challenge. In this study, we present a tactile sensing finger, UVtac, that utilizes switchable ultraviolet (UV) markers to decouple the marker and reflective membrane images to offer three-axis force estimation and object localization, whose performances are unaffected by each other. Our UVtac showed improved force estimation performance by using larger-sized UV markers through quantitative evaluation. The UVtac with 1.2 mm diameter markers showed a root mean square error of 0.264 N in estimating normal forces up to 10 N and 0.219 N in estimating the shear forces up to 5 N, when indented with an 8×8 mm^2 square tooltip. Based on the object localization experiment, the UVtac was verified to have a 31 % lower root mean square error than the case using opaque black markers. Finally, we demonstrated object alignment and contact force-tracking tasks using the UVtac to emphasize its multifunctionality.**

***Index Terms*—Perception for grasping and manipulation, force and tactile sensing, soft sensors and actuators**

I. Introduction

TACTILE perception is essential for robots to achieve various contact-rich tasks, such as dexterous object manipulation tasks [1] and collaborative tasks with physical human-robot interactions (pHRI) [2]. Therefore, robots must be equipped with tactile sensors that can reliably and accurately measure the location, direction, and magnitude of external physical stimuli. To address these requirements, tactile sensors of several transducing methods, such as piezoresistive [3], [4], piezoelectric [5], [6], capacitive [7], [8], and visual [9], have been developed.

Manuscript received: November, 16, 2021; Revised February, 17, 2022; Accepted March, 14, 2022. This letter was recommended for publication by Editor M. Vincze upon evaluation of the Associate Editor and reviewers' comments. This work is a part of the research project, "Development of core machinery technologies for autonomous operation and manufacturing (NK230G)", which has been supported by a grant from National Research Council of Science & Technology under the R&D Program of Ministry of Science, ICT and Future Planning. *(Woojong Kim and Won Dong Kim are co-first authors.) (Corresponding author: Jung Kim.)*

W. Kim, W. D. Kim, and J. Kim are with the Department of Mechanical Engineering at KAIST, Daejeon 34141, Republic of Korea (e-mail: kwjong2028@kaist.ac.kr; kwd92@kaist.ac.kr; jungkim@kaist.ac.kr)

J-J. Kim and C-H. Kim are with the Korea Institute of Machinery and Materials, Daejeon 34141, Republic of Korea (e-mail: rightcore@kimm.re.kr; chkim78@kimm.re.kr).

Digital Object Identifier (DOI): see top of this page.

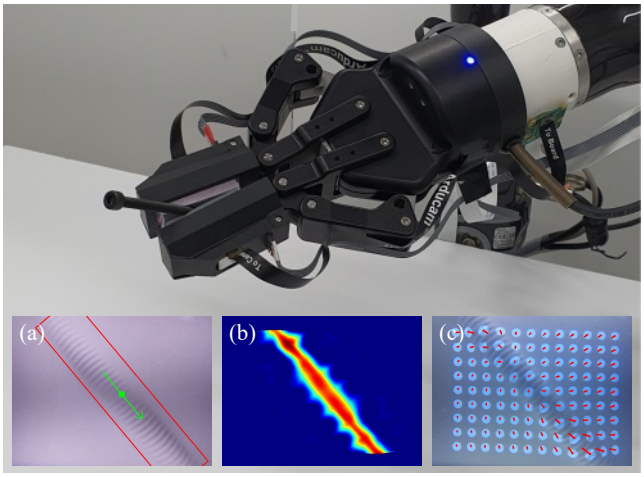

Fig. 1. Gripper equipped with the UVtac holding a bolt and respective measurement results. (a) Localization result, (b) Normal force field, (c) Marker motion field with total shear force prediction.

Among the diverse tactile sensors, vision-based tactile sensors have gained significant popularity due to the development of compact cameras with high-resolution image sensors and the evolution of image processing techniques that enable high-dimensional image data processing, even in real-time [10]. By exploiting these technological advances, vision-based tactile sensors can extract different tactile features through various operations, such as contact geometry reconstruction [11], and normal, shear, and torsional force and deformation estimation [12]–[15], as well as slip detection [16], object localization [17], and object recognition [18].

Vision-based tactile sensors can be primarily classified into two types based on the visual features of the interior of their skin surface: marker displacement-type and reflective membrane-type [10]. Marker displacement-type sensors, such as the GelForce sensor [19], [20], the TacTip family [21], [22], and the Chromatouch sensor [23], [24], infer tactile information by observing markers or elastomeric protrusions that act as markers placed on the interior of the flexible elastomer skin of the sensor. Using markers are advantageous because they require no special lighting arrangement and the shear displacement field calculation is straightforward if the skin of the sensor is flat. However, the dimension of the measured data per frame is limited by the number of markers, degrading the detailed feature extraction of the tactile stimuli.

In contrast, reflective membrane-type sensors analyze the

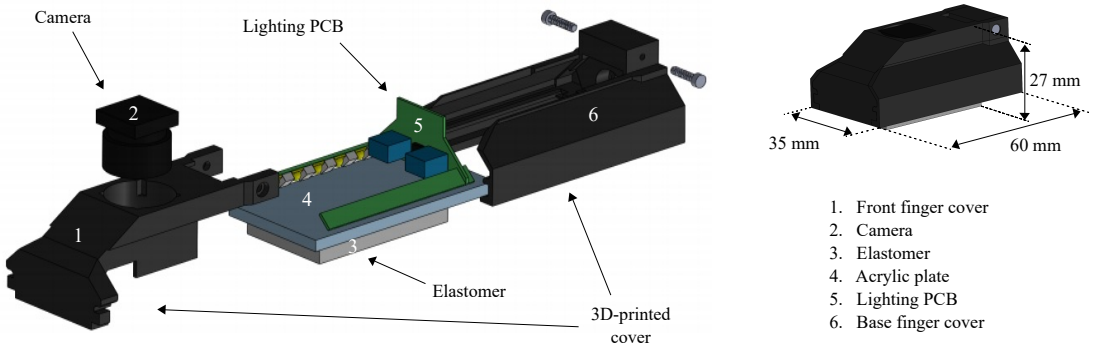

Fig. 2. Exploded diagram of UVtac and its components.

intensity change of the reflected light from the reflective membrane coated on the sensor skin. A representative of this sensor type is the GelSight sensor, currently among the most popular vision-based tactile sensor. It uses the photometric stereo [25] method, which reconstructs a heightmap with a high-spatial resolution using RGB intensity changes across the reflective membrane. Inspired by the GelSight sensor, sensors [26]–[28], such as the Digit and GelSlim sensors of various forms, have been developed. However, the downside of the reflective membrane-type is that tactile information concerning tangential forces and deformations cannot be detected and the sensor does not respond to objects without edges or textures.

Hybrid approaches, where the interior of the skin of the vision-based tactile sensor has both markers and a reflective membrane, have been proposed to implement the functions of both types of sensors together. GelSight and GelSlim sensors with markers have a slip detection function, detected by tracking the small black markers printed underneath the reflective membrane. Also, Nozu et al. [29] adopted the hybrid approach for performing bolt insertion and tightening tasks. Nozu's sensor was built by placing four large red markers on the edges of the image. Next, object localization was performed using the image of the reflective membrane, and the red markers were used to estimate the contact force.

In studies that use markers, opaque markers were used for stable marker detection under visible internal lighting. Although increasing the number or area of markers results in richer and more accurate tactile information extracted from observing markers, the ratio of the total area of opaque markers to the area of the reflective membrane increases. Since opaque markers inevitably occlude the camera's view of the reflective membrane, the quality of tactile information extracted from reflective membrane images is degraded. Such a tradeoff introduces ambiguity and restrictions in choosing the size, density, and location of the markers when designing the elastomeric skin of the sensors using the hybrid method. Abad et al. [30] addressed this issue by proposing the use of clear, ultraviolet (UV) reactive, fluorescent markers (UV markers), which are manually marked on the elastomer skin using a commercially available UV ink pen. Their study showed the advantages of using UV markers by showing contact object recognition performances under visible light and a qualitative view of optical flow under UV light. However, it has no consistent UV marking procedure and lacks quantitative analysis and comparison of replacing opaque markers with UV markers.

In this study, we present UVtac (Fig. 1), a switchable UV marker-based tactile sensing finger, which effectively addresses the tradeoffs that arise when using the hybrid method. Inspired by previous studies, we propose a UVtac design that allows the finger to be mounted on grippers, along with a consistent manufacturing process for the elastomeric skin with UV markers and reflective membrane. We devised a force estimation algorithm that utilizes the area change and tangential displacement of the UV markers to estimate the normal and shear forces in the UV light-on state (UV LED mode) and an object localization algorithm in the white light-on state (white LED mode). Furthermore, we analyzed and compared the force estimation results when using UV markers of different initial areas and validated object localization results when using different markers for quantitative evaluation. To emphasize the multifunctionality of the UVtac, the UVtac was mounted on a commercially available gripper and was used to demonstrate a robotic manipulation task and contact force-tracking tasks in the pHRI scenario.

II. Design and Fabrication

A. Design Overview

Like other vision-based tactile sensors, UVtac comprises four main components: a cover, a camera, a lighting printed circuit board (PCB), and an elastomer. The structure and dimensions of the sensor are shown in Fig. 2. The 3D-printed cover (Form 3, Formlabs) defines the overall size of the sensor. Thus, we designed the cover so that its size is suitable for use as fingers on commercial parallel grippers, while being strong enough to withstand the gripping force of 235 N (maximum gripping force of 2F-85 Adaptive Gripper, Robotiq Inc.) without breaking. The rest of the components were designed to fit tightly inside the cover.

The camera (Raspberry Pi Camera Module V2) is equipped with a fisheye lens, allowing a field of view of 220° to ensure large sensing field while maintaining compactness. The camera board is then connected to the Camera Serial Interface port on the Raspberry Pi 4B board. When the sensor is fully assembled, the lighting PCB stands right over the acrylic plate to illuminate the reflective membrane of the

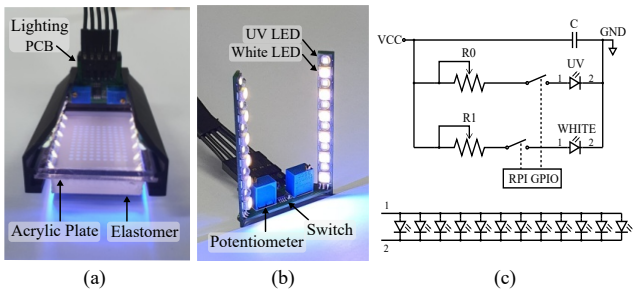

Fig. 3. (a) Assembled sensor view, (b) Lighting PCB, and (c) Circuit diagram of lighting PCB.

elastomer. The LEDs on the lighting PCB are aligned to the edges of the elastomer, slanted 45° inwards to provide even illumination across the reflective membrane. The arrangement of the components is shown in Fig. 3 (a). The lighting PCB comprises 12 white LEDs, 12 UV LEDs (peak wavelength of 365 nm), two potentiometers, and a dual Single Pole Single Throw (SPST) switch. The white and UV LEDs are placed alternately on each branched PCB (Fig. 3 (b)) to ensure even illumination across the reflective membrane regardless of the sensor mode. The white and UV LEDs form a separate parallel circuit, each connected to a potentiometer, allowing manual adjustment of the LEDs' intensities. By controlling the switch using the GPIO pins on the Raspberry Pi board, one can switch between the white and UV LED modes. Short delays are required when switching between the two modes due to communication delays at the Raspberry Pi board and light adaptation of the camera. The minimum delay times required are 15 ms and 80 ms for white to UV mode and UV to white mode changes, respectively. The circuit diagram of the lighting PCB is shown in Fig. 3 (c).

B. Elastomer Fabrication

The elastomer comprises the clear silicone base elastomer, UV markers, and reflective membrane. First, a transparent silicone rubber compound (Solaris, Smooth-On Inc., Shore hardness 15A) was used for making the clear silicone base. The mixture of the two parts of the liquid silicone was degassed and poured into a readymade mold with internal dimensions equal to the target dimensions of the elastomer skin (Fig. 4 (a), (b)).

After the base elastomer was fully cured, the UV markers were directly printed onto the elastomer using a flatbed printer (Fig. 4 (c)). The UV fluorescent ink (DigitalPoly) emits a blue light when exposed to UV rays, but remains transparent under visible light. For UVtac, circular markers forming a grid of 9 rows and 12 columns were printed, where the distance between neighboring markers is 2 mm.

The silicone paint for the reflective membrane was made by mixing a silicone paint base and color pigments (Psycho Paint and Silc Pig, Smooth-On Inc.). Next, a thinning agent (NOVOCS Gloss, Smooth-On Inc.) was added to the silicone paint to apply the membrane using an airbrush (Fig. 4 (d)). To reduce the sensor's sensitivity to external illumination, the thickness of the membrane was determined

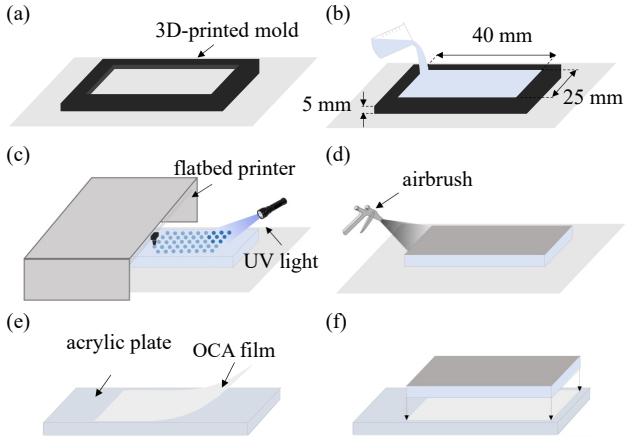

Fig. 4. Elastomer fabrication process: (a) prepare 3D-printed mold, (b) pour clear silicone rubber, (c) print UV markers using flatbed printer, (d) coat the reflective membrane using airbrush, (e) attach OCA film to acrylic plate, and (f) attach coated elastomer on the OCA film.

to be a minimum thickness of 200 µm in which the frame captured by the camera was not affected by external illumination.

Finally, the coated silicone base was pasted to an acrylic plate using an optically clear adhesive (Silicone OCA 50 µm) (Fig. 4 (e), (f)). The adhesive of the OCA film is of a silicone base, ensuring firm adhesion between the acrylic plate and the elastomer.

III. Extracting Tactile Information

A. Frame Pre-Processing

The camera streams the video frames of 1280×720 at 90 fps that have barrel distortions due to the fisheye lens. We took advantage of the fact that the markers of UVtac were printed on the flat elastomer to form an evenly spaced grid, indicating that their three-dimensional (3D) world coordinates are well-defined. Thus, the markers can be used as calibration patterns to compute the camera parameters needed for undistorting the frames. Using the centroids of the markers as the calibration patterns makes it possible to compute an undistortion map that undistorts the distortions of the raw frames (Fig. 5 (a)).

The process of determining the undistortion map only needs to be done once; the map can undistort all streaming frames in both UV and white LED modes. The undistorted frames are cropped along the region of interest (ROI) and set around the region where the UV markers are printed (Fig. 5 (a)). Then, the cropped images are resized into frames of 640×480. The resulting pre-processed frames are then processed differently based on the current sensor mode.

B. Force Estimation

We utilized the change in marker information to determine the forces acting on the elastomer. The first step to obtaining the marker information is blurring the current video frame and subtracting the blurred frame from the nonblurred current video frame. Next, a binary mask of the markers is obtained by applying a threshold in the hue saturation value (HSV) scale.

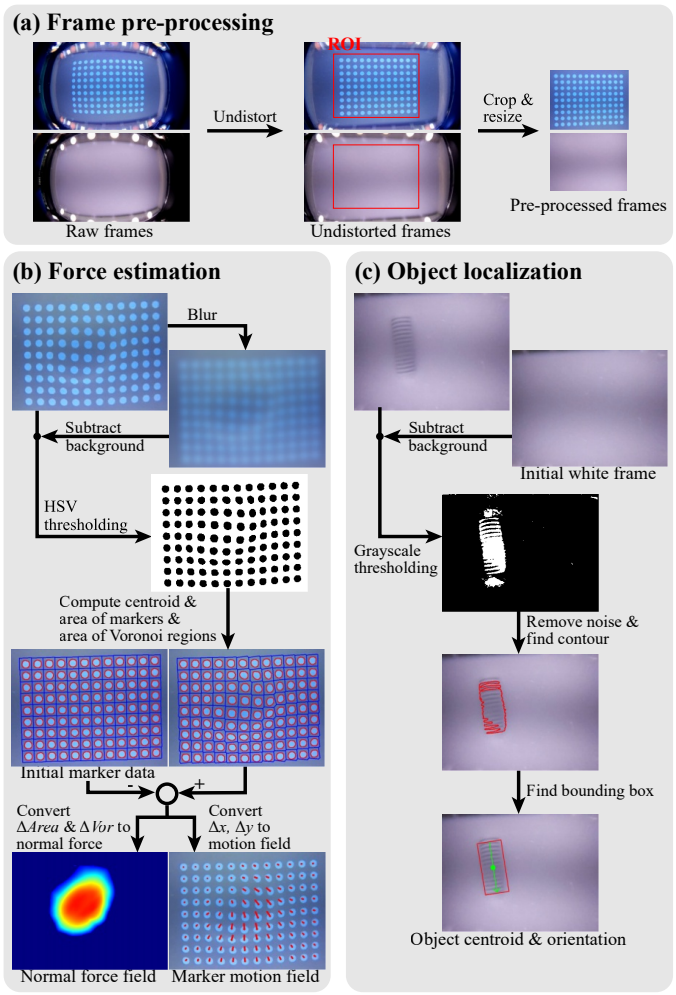

Fig. 5. Diagram of frame processing methodologies. (a) Pre-processing sequence of raw frames, (b) force estimation sequence in UV LED mode, and (c) object localization sequence in white LED mode.

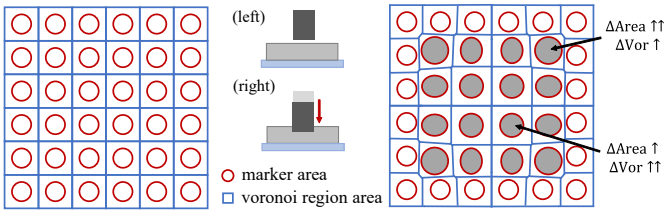

Fig. 6. Changes in marker areas (ΔArea) and Voronoi region areas (ΔVor) according to the normal compression.

The binary mask allows one to locate the contours of each marker and sequentially compute relevant marker information, such as the centroid and area of the markers. Then, the marker information in the current frame is compared to those in the initial frame, where the surface of the elastomer is undisturbed. Our proposed method uses the changes of marker information to estimate the normal and the change in total shear force acting on the elastomer.

1) Normal force field: When there is a normal deformation acting on the elastomer surface, the markers placed at the compressed region undergo a change in area due to either moving closer to the camera or stretching of the elastomer. The

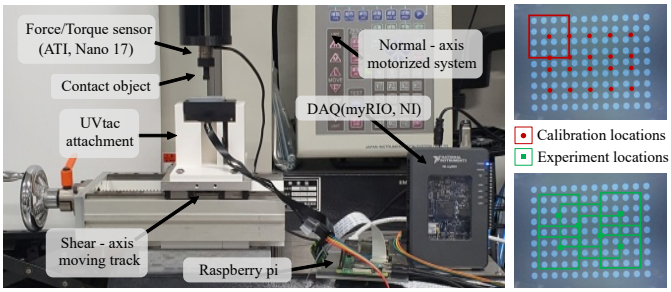

Fig. 7. (a) Experimental apparatus used to conduct force calibration and force estimation experiments, (b) Contact locations for normal force calibrations and experiments.

diagram in Fig. 6 depicts how the markers at the boundaries of the contact, where the stretching of the elastomer is dominant, undergo a larger change in area compared to those at the interior of the contact. Therefore, if the change in marker area is solely used to estimate normal forces, it produces a distorted distribution of normal forces, where the normal forces are excessively concentrated at the boundaries of the contact.

To account for the shortcoming of using only marker areas for estimating normal forces, we also consider the changes in distances between the marker centroid with its neighboring marker centroids. The change in distances to neighboring markers differ depending on whether the neighboring markers lie within or outside the contact region (Fig. 6), and thus, can be used as a geometric variable for distinguishing the main cause of the change in marker area. Instead of considering the distances to the neighboring markers as a multi-dimensional variable for each marker, we produce a Euclidean distance-based Voronoi diagram with the marker centroids as seed points, and assign the area of the Voronoi region associated with the marker centroid as a variable that acts as a comprehensive indicator of the distances to neighboring markers. Using both the marker areas and the Voronoi region areas, it is possible to estimate normal forces with a mapping function, f, as follows:

$$F_i = f(x_i, y_i, \Delta A_i, \Delta Vor_i), \tag{1}$$

where x_i, y_i, A_i, Vor_i are the horizontal and vertical centroids, area of the i^{th} marker and its associated Voronoi region area, and F_i is the normal force acting on the corresponding marker.

The normal force calibrations are performed using the setup shown in Fig. 7 (a). The setup is composed of a six-axis force-torque (F/T) sensor (Nano 17, ATI) to which the contact tooltip (square of 8 mm length) is attached, a data acquisition unit (myRIO, National Instruments) for recording the outputs from the F/T sensor, and a motorized system (HIT-B, JISC) with an integrated z-axis force sensor that allows the indenter to move based on either its position or the normal force acting on the indenter. For the normal force calibration, the elastomer was indented at 20 different locations (Fig. 7 (b)) at force intervals of 2 N from 0 to 12 N (maximum indentation depth of 1.2 mm). Each interval was assumed to be quasi-static deformation, as the tooltip was left still for sufficient time at each

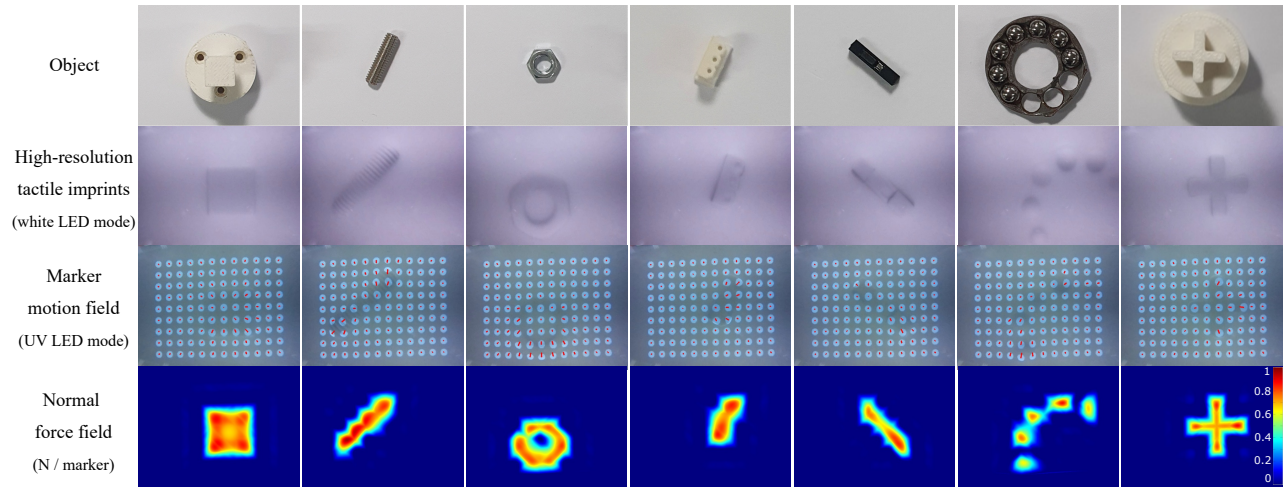

Fig. 8. Various objects under test and corresponding measurements taken using UVtac.

interval to minimize the viscoelastic effect of the elastomer. At each interval, the centroids, area of markers, and area of the Voronoi regions of the markers within the contact region were recorded, along with the force per marker, which is the normal force value measured by the F/T sensor divided by the number of markers within the contact region. Multivariate polynomial regression using a third-degree polynomial in four variables, x, y, ΔA, and ΔVor, was performed on the recorded data to obtain the mapping function in Eq. (1).

The normal forces calculated from Eq. (1) are interpolated across the entire image to generate a normal force field. Finally, the K-means clustering algorithm of $K = 2$ was used to separate the values due to normal compression from the noises. Examples of normal force fields can be seen in the last row of Fig. 8.

2) Marker motion field and change in total shear force: The marker motion field is directly computed from the change in marker centroids, Δx_i and Δy_i. Examples of marker motion fields can be seen in the third row of Fig. 8. Since marker displacements occur due to both external shear and internal forces, direct estimation of shear force field from marker motion field can lead to an unrealistic approximation of the shear force acting on each marker [13]. Instead of estimating the shear force field, with appropriate calibrations and mapping function, g, it is possible to determine the change in total shear force vector from the sum of marker motion vectors as follows:

$$\Delta\vec{\boldsymbol{V}} = g\left(\sum_{i=1}^{N}(\Delta x_i\hat{\boldsymbol{\imath}} + \Delta y_i\hat{\boldsymbol{\jmath}})\right), \tag{2}$$

where x_i and y_i are the horizontal and vertical centroids, N is the total number of markers, and $\vec{\boldsymbol{V}}$ is the total shear force vector acting on the entire elastomer.

A similar setup to that used for normal force calibration was used for calibrating changes in total shear force, with an addition of a moving track that allows the base to which the sensor is attached to move in the tangential direction. The elastomer was precompressed in the normal direction by 0.5 mm to prevent slip, and marker centroids at this state were recorded as the initial marker positions. Then, shear forces were generated by moving the shear-axis moving track. The shear force measured by the F/T sensor and the displacements of the marker centroids were recorded up to a shear force change of 5.5 N at a single point to compute the mapping function in Eq. (2).

C. Object Localization

The process for localizing the contact made by an object on the elastomer in the white LED mode is shown in Fig. 5 (c). First, the background of the current frame, such as the images in the second row of Fig. 8, is removed by subtracting the initial frame, which is the frame when the surface of the elastomer is unperturbed. Then, the resulting image is converted to a grayscale image. A binary threshold is applied on the grayscale image to extract a mask of the contact. The threshold value was set to 10 on a scale from 0 to 255, which is the baseline noise level of the background when images of unperturbed elastomer were converted to grayscale images.

From the mask, it is possible to find the contours of the contact. In this process, noises caused by shadows, which are significant when the contacts have a sharp edge, are misleadingly captured as contacts. Therefore, contours with small contour areas are neglected to remove the noises. Then, a minimum bounding box of the noise-removed contour is computed, along with its centroid position and orientation. Our object localization method takes the centroid position and orientation of the minimum bounding box as the position and orientation of the object relative to the sensor.

IV. Experimental Results

A. Force Estimation Experiment

The performance of the force estimation of the proposed tactile sensor was examined using force estimation experiments. The setup for the experiments is identical to the setup used for force calibrations (Fig. 7 (a)). The F/T sensor, whose force outputs are used as the ground-truth value, does not measure force distributions. Therefore, to quantitatively evaluate the normal force estimation performance of UVtac against the F/T

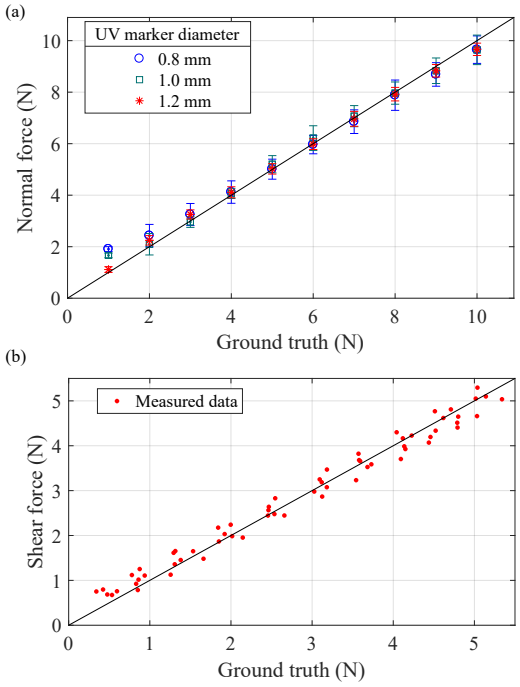

Fig. 9. Results of (a) normal and (b) shear force estimation experiment.

TABLE I
RESULTS OF THE NORMAL FORCE ESTIMATION EXPERIMENT

UV marker diameter (mm)	Average standard deviation (N)	Root mean square error (RMSE) (N)
0.8	0.418	0.541
1.0	0.363	0.445
1.2	0.213	0.264

sensor output, the estimated normal force at each marker is summed up, $\sum_{i=1}^{N} F_i$, to compute the total normal force acting on the elastomer. In the normal force estimation experiment, three elastomers with the same number of UV markers, but different marker diameters of 0.8, 1.0, and 1.2 mm, were used. The UVtac elastomers were pressed at six contact points that were not used as calibration points, shown in Fig. 7 (b), at force intervals of 1 N from 0 to 10 N. As was done during calibration, quasi-static procedures were performed at each interval.

The results of the normal force estimation experiment are shown in Fig. 9 (a) and Table I. The data show that the average standard deviation and the root mean square error (RMSE) decrease as the size of the UV markers increases. This trend occurs because the larger markers have less sensitivity to noise occurring due to fluctuations in marker area detection. Additionally, large estimation errors were seen when estimating small normal forces due to the difficulty in distinguishing the actual contact and noise using the K-means clustering. This effect also decreases as the size of the UV marker increases due to the decreased noise level mentioned above. Overall, the case of the 1.2 mm marker with the best force estimation result was selected as the marker diameter of UVtac. This experiment not only confirmed that using UV ink for markers allows the design of markers without being limited by the size of the markers but also verified that using larger markers improves the normal force estimation performances.

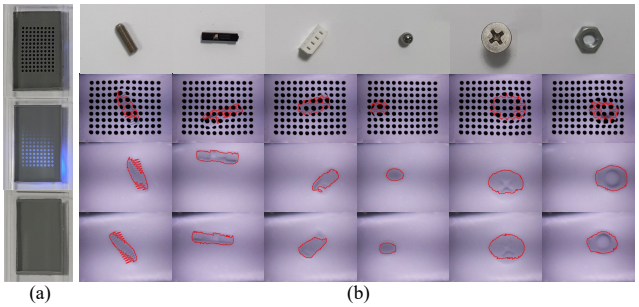

Fig. 10. (a) Elastomers used in object localization experiments *(from top to bottom)*: black, UV, and no marker elastomer. (b) Objects selected for object localization experiment *(from left to right)*: bolt, jumper cable head, pin connector, metal ball, bolt head, and nut. Contours of objects in contact with *(from top to bottom)* black, UV, and no marker elastomers.

Subsequently, the shear force estimation experiment was performed on the selected elastomer with a marker diameter of 1.2 mm. Similar to the calibration process, the elastomer was precompressed in the normal direction by 0.5 mm at each contact locations shown in Fig. 7 (b). The change in total shear forces were estimated at the six experiment contact locations for ten to eleven different shear forces per location. The magnitude of the change in total shear, $\|\Delta\vec{V}\|$ was used to compare against the magnitude of the lateral force outputs of the F/T sensor. The experiment results are shown in Fig. 9 (b). The estimations of the UVtac are close to the identity line, and the RMSE was 0.219 N.

B. Object Localization

An object localization experiment was conducted to evaluate the performance of localizing objects in contact with the sensor and compare the performance with elastomers that use black ink for markers. In this experiment, the sensor was equipped with three different elastomers (Fig. 10 (a)): elastomers with black, UV, and no markers, respectively. The diameters of the black and UV markers were both 1.2 mm. As shown in Fig. 10 (b), six different daily objects were pressed onto the elastomers at random positions and orientations for a maximum of 20 times per object. The ground-truth positions and orientations of the contacted objects were labeled from the captured images and compared with the estimated positions and orientations computed from the object localization method described in Section III-C.

For the elastomers with black markers, the object localization method was modified to remove the markers during image processing. After the background subtraction, where the initial frame is directly subtracted from the current frame, the pixels coinciding with either the markers of the current or the initial frame were changed to black pixels. The rest of the object localization method follows that of Section III-C.

The results of the object localization experiment are shown in Fig. 11. The estimation of the object positions was generally more accurate in the elastomers with UV and no markers than in the elastomers with black markers (Fig. 11 (a)); the

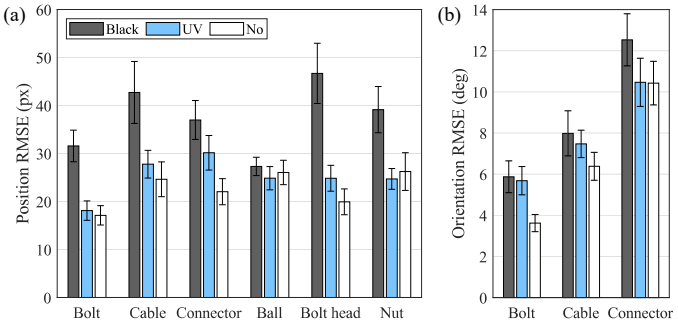

Fig. 11. RMSE between real and estimated (a) positions and (b) orientations of selected objects.

average RMSE was 31 % lower in the case with UV markers than that with black markers. Additionally, the localization error between the elastomers with UV markers and no markers showed little difference. For smaller objects, the localization error between the different elastomers showed similar error values, while objects of larger contact areas, showed increased localization errors when opaque markers existed. This is due to larger contact area leading to overlapping more markers, losing more of its contact contours due to markers.

Since the shapes of the ball, bolt head, and nut have no definite major axis against which the orientation can be defined, the evaluation of the estimations for the orientations was performed only with the other three objects. The error in estimating the object orientation is the highest in the elastomer with black markers (Fig. 11 (b)); the mean RMSE was 10 % higher in the case with black markers compared to that with UV markers. Object localization experiment results show that using UV markers increases the object localization performance compared to using black markers.

C. UVtac Usage Demonstration

To demonstrate how UVtac can be used in real-world scenarios, the UVtac was mounted on a robotic manipulator system. The manipulator system comprises a robotic arm (Jaco2 7-Dof, Kinova Inc.) with a two-fingered gripper (2F-85 Adaptive Gripper, Robotiq Inc.) attached as the end effector, where the fingertips are replaced with UVtac.

Here, we present object alignment and force-tracking tasks as demonstrations. In the object alignment task, the UVtac is operated in the white LED mode. First, the robot is handed over with an object to grip. Then, the in-hand orientation of the object is computed from the tactile frames. The rotational motion necessary for the object to reach the target orientation is computed using the in-hand orientation of the object and end effector orientation. The scenes of the robot performing the object alignment task are shown in Fig. 12 (a).

The UVtac is operated in the UV LED mode in the force-tracking task (Fig. 12 (b)). In this task, the manipulator performs translational motions according to the change in the three-axis force vector computed from the markers. First, the gripper grasps an object and the normal and shear tactile forces at equilibrium are saved. Then, when external forces are applied on the object, the change in force vector with respect

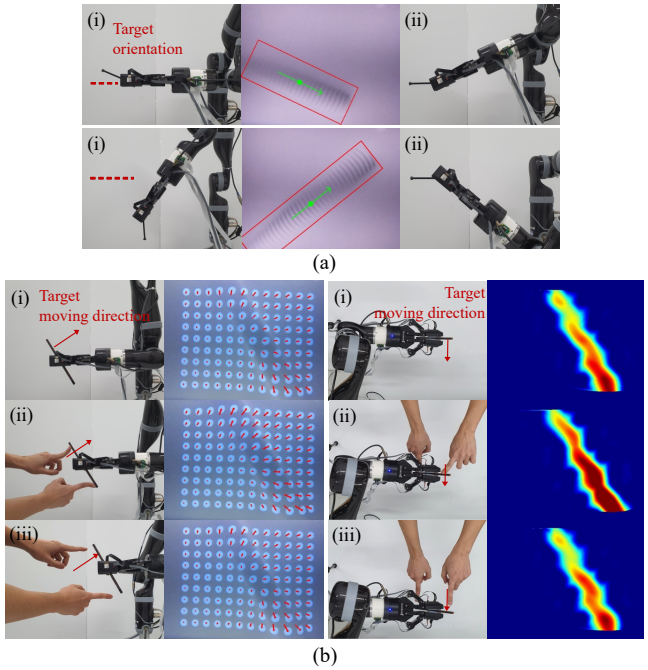

Fig. 12. Captured scenes during (a) bolt alignment task with object localization measurements and (b) contact force-tracking task using normal and shear force estimates.

to the forces at equilibrium is computed. The manipulator moves toward the direction of the change of the force vector. Fig. 12 (b) shows the scenes of the robot performing the force-tracking task, reacting to both normal and shear tactile force changes.

V. Discussion and Conclusion

We proposed a novel UVtac tactile sensor design, which provides switchable modes to address the tradeoff problem in conventional hybrid vision-based tactile sensors. Furthermore, an algorithm was implemented that can perform different functions in each LED mode; the three-axis force estimation is performed in the UV LED mode and the object localization is performed in the white LED mode. Compared to previous works where the centroids of the markers were mainly used to estimate forces [14], [20], [21], we proposed a new normal force field estimation method that exploits the advantage of using UV markers by using marker areas and Voronoi region areas. The quantitative analysis from the experiments shows that it is possible to increase the quality of both marker-based and reflective membrane-based tactile information using switchable UV markers. Moreover, a consistent manufacturing process was provided for fabricating elastomers with UV markers and a compact design that allows UVtac to be used as fingertips in commercially available grippers. Consequently, our UVtac has comparable compactness, sensing field, image resolution, and frame rate compared to other prominent vision-based tactile sensors, but weighs only 39 g (Table II). Additionally, it was demonstrated that the sensor can be utilized for manipulation and pHRI tasks.

Nevertheless, there are several drawbacks to be addressed. Due to the divided LED modes, a well-defined finite state

TABLE II
COMPARISON OF UVTAC, GELSLIM, GELSIGHT, AND DIGIT

	Size (mm)	Weight (g)	Sensing Field (mm^2)	Image Resolution	Image fps
UVtac (ours)	$35 \times 60 \times 27$	39	588		90
GelSlim 3.0 [31]	$37 \times 80 \times 20$	45	675		90
GelSlim 2.0 [13]	$50 \times 172 \times 25$	222	1200	640×480	90
GelSight [11]	$40 \times 80 \times 40$	NA	252		30
Digit [26]	$20 \times 27 \times 18$	20	304		60

machine for mode switching is needed in more complex manipulation tasks. Due to the delays in switching modes mentioned in Section II-A, simultaneous use of the two modes is limited to 10 fps. Additionally, the shear force estimation method presented in this work is limited to estimating the change in the total shear force acting on the elastomer, due to the marker displacements caused by internal forces in the deformed elastomer. Therefore, there is room for improving the current shear force estimation methods by supplementing the method with means of distinguishing marker movements caused by external shear and internal forces. One possible method would be to use the contact shape detected in the white LED mode and use it as a geometric constraint in distributing the measured normal and shear force values. Major future work is to devise higher-level control schemes specific to robot systems mounted with UVtac to perform various real-world object manipulation scenarios.

REFERENCES

[1] Q. Li, O. Kroemer, Z. Su, F. F. Veiga, M. Kaboli, and H. J. Ritter, "A review of tactile information: Perception and action through touch," *IEEE Transactions on Robotics*, vol. 36, no. 6, pp. 1619–1634, 2020.

[2] R. S. Dahiya, P. Mittendorfer, M. Valle, G. Cheng, and V. J. Lumelsky, "Directions toward effective utilization of tactile skin: A review," *IEEE Sensors Journal*, vol. 13, no. 11, pp. 4121–4138, 2013.

[3] R. Kõiva, M. Zenker, C. Schürmann, R. Haschke, and H. J. Ritter, "A highly sensitive 3d-shaped tactile sensor," in *2013 IEEE/ASME International Conference on Advanced Intelligent Mechatronics*, 2013, pp. 1084–1089.

[4] M. Strohmayr, H. Saal, A. Potdar, and P. van der Smagt, "The dlr touch sensor i: A flexible tactile sensor for robotic hands based on a crossed-wire approach," in *2010 IEEE/RSJ International Conference on Intelligent Robots and Systems*, 2010, pp. 897–903.

[5] D. Goger, N. Gorges, and H. Worn, "Tactile sensing for an anthropomorphic robotic hand: Hardware and signal processing," in *2009 IEEE International Conference on Robotics and Automation*, 2009, pp. 895–901.

[6] B. Choi, S. Lee, H. R. Choi, and S. Kang, "Development of anthropomorphic robot hand with tactile sensor : Skku hand ii," in *2006 IEEE/RSJ International Conference on Intelligent Robots and Systems*, 2006, pp. 3779–3784.

[7] A. Schmitz, M. Maggiali, L. Natale, B. Bonino, and G. Metta, "A tactile sensor for the fingertips of the humanoid robot icub," in *2010 IEEE/RSJ International Conference on Intelligent Robots and Systems*, 2010, pp. 2212–2217.

[8] P. A. Schmidt, E. Maël, and R. P. Würtz, "A sensor for dynamic tactile information with applications in human–robot interaction and object exploration," *Robotics and Autonomous Systems*, vol. 54, no. 12, pp. 1005–1014, 2006.

[9] A. C. Abad and A. Ranasinghe, "Visuotactile sensors with emphasis on gelsight sensor: A review," *IEEE Sensors Journal*, vol. 20, no. 14, pp. 7628–7638, 2020.

[10] K. Shimonomura, "Tactile image sensors employing camera: A review," *Sensors*, vol. 19, no. 18, p. 3933, 2019.

[11] S. Dong, W. Yuan, and E. H. Adelson, "Improved gelsight tactile sensor for measuring geometry and slip," in *2017 IEEE/RSJ International Conference on Intelligent Robots and Systems (IROS)*. IEEE, 2017, pp. 137–144.

[12] W. Yuan, S. Dong, and E. H. Adelson, "Gelsight: High-resolution robot tactile sensors for estimating geometry and force," *Sensors*, vol. 17, no. 12, p. 2762, 2017.

[13] D. Ma, E. Donlon, S. Dong, and A. Rodriguez, "Dense tactile force estimation using gelslim and inverse fem," in *2019 International Conference on Robotics and Automation (ICRA)*. IEEE, 2019, pp. 5418–5424.

[14] A. Yamaguchi and C. G. Atkeson, "Combining finger vision and optical tactile sensing: Reducing and handling errors while cutting vegetables," in *2016 IEEE-RAS 16th International Conference on Humanoid Robots (Humanoids)*. IEEE, 2016, pp. 1045–1051.

[15] Y. Zhang, Z. Kan, Y. Yang, Y. A. Tse, and M. Y. Wang, "Effective estimation of contact force and torque for vision-based tactile sensors with helmholtz–hodge decomposition," *IEEE Robotics and Automation Letters*, vol. 4, no. 4, pp. 4094–4101, 2019.

[16] W. Yuan, R. Li, M. A. Srinivasan, and E. H. Adelson, "Measurement of shear and slip with a gelsight tactile sensor," in *2015 IEEE International Conference on Robotics and Automation (ICRA)*. IEEE, 2015, pp. 304–311.

[17] R. Li, R. Platt, W. Yuan, A. ten Pas, N. Roscup, M. A. Srinivasan, and E. Adelson, "Localization and manipulation of small parts using gelsight tactile sensing," in *2014 IEEE/RSJ International Conference on Intelligent Robots and Systems*. IEEE, 2014, pp. 3988–3993.

[18] J. Lin, R. Calandra, and S. Levine, "Learning to identify object instances by touch: Tactile recognition via multimodal matching," in *2019 International Conference on Robotics and Automation (ICRA)*, 2019, pp. 3644–3650.

[19] K. Kamiyama, K. Vlack, T. Mizota, H. Kajimoto, K. Kawakami, and S. Tachi, "Vision-based sensor for real-time measuring of surface traction fields," *IEEE Computer Graphics and Applications*, vol. 25, no. 1, pp. 68–75, 2005.

[20] K. Sato, K. Kamiyama, N. Kawakami, and S. Tachi, "Finger-shaped gelforce: sensor for measuring surface traction fields for robotic hand," *IEEE Transactions on Haptics*, vol. 3, no. 1, pp. 37–47, 2009.

[21] B. Winstone, G. Griffiths, C. Melhuish, T. Pipe, and J. Rossiter, "Tactip—tactile fingertip device, challenges in reduction of size to ready for robot hand integration," in *2012 IEEE International Conference on Robotics and Biomimetics (ROBIO)*. IEEE, 2012, pp. 160–166.

[22] B. Ward-Cherrier, N. Pestell, L. Cramphorn, B. Winstone, M. E. Giannaccini, J. Rossiter, and N. F. Lepora, "The tactip family: Soft optical tactile sensors with 3d-printed biomimetic morphologies," *Soft robotics*, vol. 5, no. 2, pp. 216–227, 2018.

[23] X. Lin and M. Wiertlewski, "Sensing the frictional state of a robotic skin via subtractive color mixing," *IEEE Robotics and Automation Letters*, vol. 4, no. 3, pp. 2386–2392, 2019.

[24] X. Lin, L. Willemet, A. Bailleul, and M. Wiertlewski, "Curvature sensing with a spherical tactile sensor using the color-interference of a marker array," in *2020 IEEE International Conference on Robotics and Automation (ICRA)*. IEEE, 2020, pp. 603–609.

[25] M. K. Johnson and E. H. Adelson, "Retrographic sensing for the measurement of surface texture and shape," in *2009 IEEE Conference on Computer Vision and Pattern Recognition*. IEEE, 2009, pp. 1070–1077.

[26] M. Lambeta, P.-W. Chou, S. Tian, B. Yang, B. Maloon, V. R. Most, D. Stroud, R. Santos, A. Byagowi, G. Kammerer *et al.*, "Digit: A novel design for a low-cost compact high-resolution tactile sensor with application to in-hand manipulation," *IEEE Robotics and Automation Letters*, vol. 5, no. 3, pp. 3838–3845, 2020.

[27] E. Donlon, S. Dong, M. Liu, J. Li, E. Adelson, and A. Rodriguez, "Gelslim: A high-resolution, compact, robust, and calibrated tactile-sensing finger," in *2018 IEEE/RSJ International Conference on Intelligent Robots and Systems (IROS)*. IEEE, 2018, pp. 1927–1934.

[28] B. Romero, F. Veiga, and E. Adelson, "Soft, round, high resolution tactile fingertip sensors for dexterous robotic manipulation," in *2020 IEEE International Conference on Robotics and Automation (ICRA)*. IEEE, 2020, pp. 4796–4802.

[29] K. Nozu and K. Shimonomura, "Robotic bolt insertion and tightening based on in-hand object localization and force sensing," in *2018 IEEE/ASME International Conference on Advanced Intelligent Mechatronics (AIM)*. IEEE, 2018, pp. 310–315.

[30] A. C. Abad and A. Ranasinghe, "Low-cost gelsight with uv markings: Feature extraction of objects using alexnet and optical flow without 3d image reconstruction," in *2020 IEEE International Conference on Robotics and Automation (ICRA)*. IEEE, 2020, pp. 3680–3685.

[31] I. Taylor, S. Dong, and A. Rodriguez, "Gelslim 3.0: High-resolution measurement of shape, force and slip in a compact tactile-sensing finger," *arXiv preprint arXiv:2103.12269*, 2021.